AIP Journal of Applied Physics

Evolution of catalyst particle size during carbon single walled nanotube growth and its effect on the tube characteristics

Avetik R. Harutyunyan, Toshio Tokune, Elena Mora, Jung-Woo Yoo, and Arthur J. Epstein

Citation: Journal of Applied Physics **100**, 044321 (2006); doi: 10.1063/1.2335396
View online: http://dx.doi.org/10.1063/1.2335396
View Table of Contents: http://scitation.aip.org/content/aip/journal/jap/100/4?ver=pdfcov
Published by the AIP Publishing

Evolution of catalyst particle size during carbon single walled nanotube growth and its effect on the tube characteristics

Avetik R. Harutyunyan[a] and Toshio Tokune
Honda Research Institute USA Inc., 1381 Kinnear Road, Columbus, Ohio 43212

Elena Mora, Jung-Woo Yoo, and Arthur J. Epstein
Department of Physics, The Ohio State University, 191 West Woodruff Avenue, Columbus, Ohio 43210-1117 and Department of Chemistry, The Ohio State University, 100 West 18th Avenue, Columbus, Ohio 43210-1173

(Received 9 January 2006; accepted 11 July 2006; published online 30 August 2006)

A series of Fe catalysts, with different mean diameters, supported on alumina with different molar ratios, was studied before and after carbon single walled nanotubes growth using magnetic measurements and Raman scattering techniques (laser excitation wavelengths from 1.17 to 2.54 eV) to follow changes on catalyst particle size and composition, as well as the relationship between particle size and diameter of nanotubes grown. In all cases, an increase and redistribution of the particle size after the growth was concluded based on the blocking temperature values and Langevin function analysis. This is explained in terms of agglomeration of particles due to carbon-induced liquefaction accompanied with an increase in the catalyst mobility. For large particles no direct correlation between the catalyst size and the nanotube diameters was observed. © *2006 American Institute of Physics*. [DOI: 10.1063/1.2335396]

I. INTRODUCTION

Many potential applications of carbon single walled nanotubes (SWNTs) require reasonably homogeneous (diameter and chirality) materials.[1] Even though extensive effort has been made to control the diameter, chirality, and type (metallic or semiconducting) of the nanotubes, by varying the catalyst size and composition, support/substrate materials, synthesis temperature, and hydrocarbon gases,[2–12] synthesis of nanotubes with given characteristics is still very challenging. The size of catalyst particles is one of the key issues in the growth of SWNTs. Transmission electron microscope (TEM) images of catalyst particles at the ends of the nanotubes have been used to show that diameter of nanotubes is determined by initial catalyst particle size.[2,13,14] A similar conclusion has been presented based on the diameter of grown nanotubes (d) and the nearly monodisperse initial Fe catalyst size (R).[15] Meanwhile, no relationship has been established between particle size and nanotube diameter grown on isolated Fe nanoparticles.[16] Moreover, the growth of nanotubes with diameters from 0.6 to 2 nm with catalyst sizes varying from 1 to 3 nm has been reported lately.[17] Therefore, for a controllable synthesis it is crucial to reveal the role of the catalyst size on the nanotube diameter and chirality. For this purpose, among the established nanotube growth methods, the chemical vapor deposition (CVD) is the most suitable. However, the use of TEM for direct study of catalyst nanoparticle sizes and their evolution during SWNT growth by CVD is extremely difficult, as the small catalyst particles are buried inside the pores of the support material.

In the present work, combining magnetic and Raman measurements we studied the change of the catalyst particle size and composition during carbon SWNT growth by CVD, and the relationship between particle size and the corresponding nanotube diameter. In general, we observed that the catalyst particle size and its composition vary during the nanotube growth due to carbon-induced liquefaction, creating difficulties to control the growth by controlling the initial catalyst diameters, unless appropriate interfacial interaction between catalyst and support is provided. Moreover, for relatively big catalyst particles, the nanotube diameter is not necessarily the same as the catalyst diameter.

II. EXPERIMENTAL METHOD

Four different groups of catalyst particles were synthesized and used for the growth of SWNTs by CVD. Two groups of narrowly dispersed iron catalysts, with average diameters of 8 and 4.5 nm (further in the text referred as samples S1 and S2, respectively), were obtained by thermal decomposition of iron acetate in glycol solution under nitrogen atmosphere (Fig. 1).[18] The reaction time and iron acetate/glycol ratio were changed to control the size of the nanoparticles.[18] After the nanoparticles were formed, aluminum oxide powder was added to the solution (molar ratio $Fe:Al_2O_3=1:8.5$). The solution was then stirred for 4 h, followed by the evaporation of the solvent under a flow of nitrogen gas. The third and fourth groups of catalysts were prepared by a common wet catalyst method, using iron (II) sulphate and alumina support powder with molar ratios $Fe:Al_2O_3$ of 1:14 (S3) and 1:15 (S4), with the *in situ* formation of the iron nanoparticles inside the pores of the support. This method provides good dispersion of the catalyst particles and is very convenient and inexpensive for large-scale production of carbon SWNTs. The particles were calcined at 450 °C for 2 h and then heat treated under Ar gas flowing at 820 °C (same condition as SWNT growth only without pro-

[a]Electronic mail: aharutyunyan@honda-ri.com

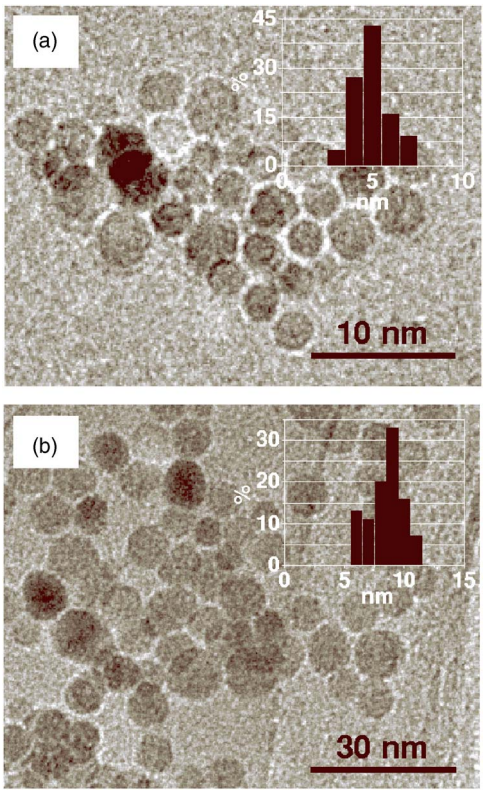

FIG. 1. TEM micrographs showing nearly spherical Fe oxide nanoparticles with mean diameters: (a) 4.5 and (b) 8 nm. The inset in each panel is the histogram of the particle diameter distribution.

viding hydrocarbon gas). The particular $Fe:Al_2O_3$ molar ratios of 1:14 and 1:15 were chosen because they are very common and give relatively high carbon SWNT yield (see Ref. 10).

The CVD growth of SWNTs at 820 °C, using methane as carbon source [gas flow rate 60 SCCM (SCCM denotes cubic centimeter per minute at STP)], was performed as described elsewhere.[6] Prior to the introduction of the hydrocarbon gas, the catalyst particles were reduced under H_2/He gas mixture at 500 °C.

A superconducting-quantum-interference-device (SQUID) magnetometer (MPMS, Quantum Design) was used to follow particle evolution to fields up to 55 kG, in the temperature range of 5–300 K. Recently, magnetic measurements were used for characterization of impurities in a SWNT sample.[19]

Raman spectra were collected using a Bomem DA3 +FT spectrometer with Nd:YAG (yttrium aluminum garnet) laser excitation 1.17 eV ($\lambda = 1064.5$ nm). A JY-ISA HR460 single grating spectrometer with charge-coupled device (CCD) detector and a holographic notch filter (Kaiser Optical) was used to collect spectra with 2.54 eV (488 nm), 2.41 eV (514.5 nm), and 1.92 eV (647.1 nm) excitations (mixed gas Ar–Kr ion laser). The Raman spectra for 532 and 785 nm excitations were collected in a Thermo Nicolet Almega Raman spectrometer equipped with a CCD detector.

Transmission electron microscopy (Philips CM300 Ultra-Twin FEG) was used for further characterization of the SWNT samples.

III. RESULTS AND DISCUSSION

A. Magnetic characterization of initial catalysts

The wet chemistry method used to prepare samples 3 and 4 is one of the most common approaches for the preparation of supported catalyst particles for CVD growth of SWNT. Because of the *in situ* formation of the nanoparticles inside the pores of the support material, it is impossible to directly verify the particle size by TEM. Magnetic characterization of the catalyst particles can be an alternative tool for nondestructive evaluation of particle size before and after SWNT growth. To support this approach, we use the magnetic characterization data of specially prepared samples 1 and 2, with well-defined diameters measured by TEM, to interpret and validate the magnetic data of samples 3 and 4.

The magnetization curves of the four different groups of iron oxide catalysts supported on Al_2O_3 powder are shown in Fig. 2. The iron oxide particles with diameters of 8 nm (S1) and 4.5 nm (S2) supported on Al_2O_3 (molar ratio 1:8.5) and prepared from solution with molar ratio 1:14 (S3) showed hysteresis loops with characteristic values of remnant magnetization (M_r) and coercivity at 5 K, while at room temperature no hysteresis loop was detected. This magnetic behavior is well described in terms of superparamagnetism in nanoparticles with size less than single domain particle regime (<20 nm for Fe). A distinguishing feature of S3 is the increase in the magnetization without saturation with the increase of the applied magnetic field up to 55 kG at 300 K. Decreasing the Fe content to a molar ratio 1:15 (S4) leads to nonsaturated magnetic curves in all the temperature range studied (5–300 K). Taking into account the paramagnetic behavior of S4 and the fact that the saturation of magnetization (M_s) decreases from 131 to 102 and 70 emu/g for samples S1, S2, and S3, respectively (Fig. 2), we conclude that decreasing of $Fe:Al_2O_3$ ratio leads to a decrease of particle size $d_1 > d_2 > d_3 > d_4$.

The magnetic characterization provides also information about catalyst particle composition. The M_s value for pure bulk Fe is ~220 emu/g. It is established that the oxide layers can be present as nonmagnetic shell,[20] superparamagnetic due to very fine grain size,[21] ferromagnetic with a noticeable M_s of 45 emu/g,[22] or as ferromagnetic with 80 emu/g (M_s of bulk Fe oxide). Therefore, the magnetic contribution from the oxide surface layers around the particle can vary from 0 to 80 emu/g. Hence, the observed values of M_s can be attributed to the presence of an iron oxide shell on the pure Fe core, with different thicknesses (different fractions of iron oxide) depending on the particle size, which is consistent with particle preparation method (calcinations under flowing air). For S1, a magnetization of 131 emu/g results in the variation of pure iron content in the particle from 59.5 wt. % Fe coated with 40.5 wt. % of nonmagnetic oxide layer to 36 wt. % Fe and 64 wt. % iron oxide, depending on the magnetic state of the oxide layer. Taking into account the particle mean diameter determined by TEM (8 nm), the density of the Fe core (7.86 g/cm^3) and the density of the oxide shell (5.23 g/cm^3), we obtained that the Fe core diameter varies from 6.24 to 5.0 nm, when Fe–O thickness changes from 0.88 to 1.5 nm, respectively. For S2 with mean particle size

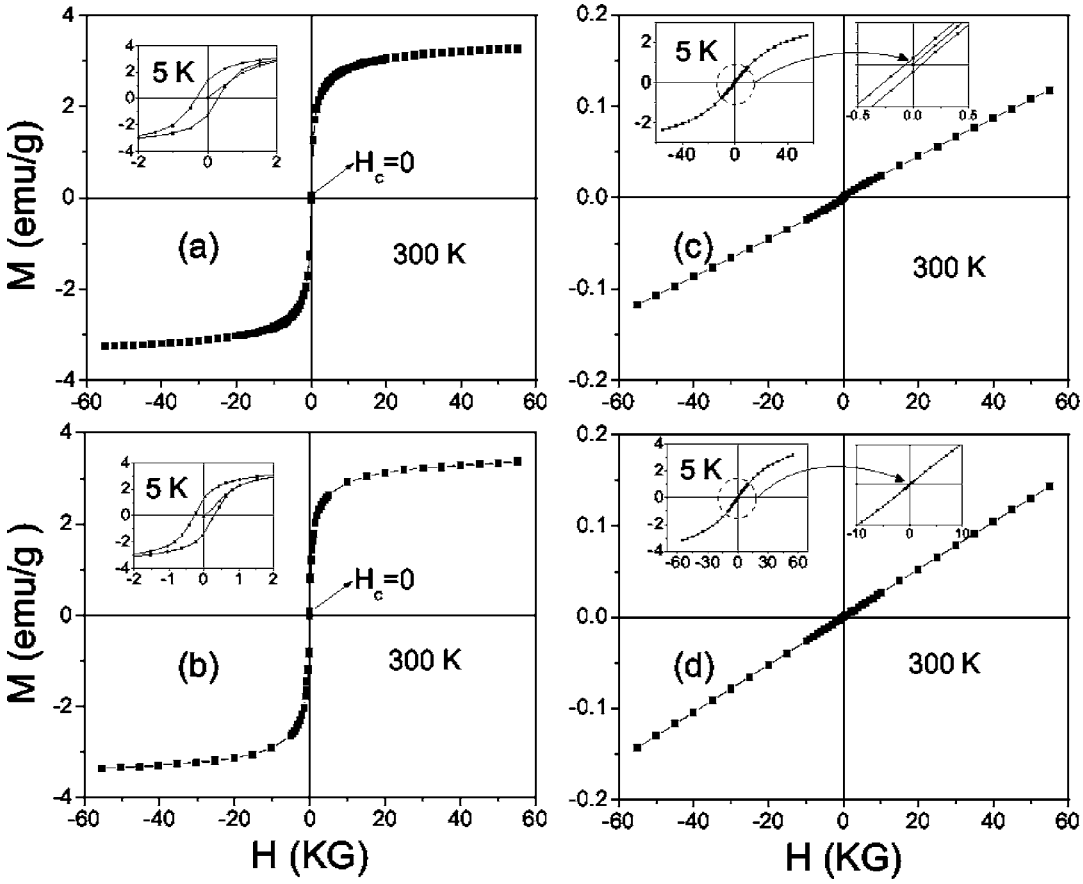

FIG. 2. Magnetization curves of the alumina supported Fe oxide nanoparticles before carbon SWNT growth at 300 and 5 K corresponding to samples (a) 1, (b) 2, (c) 3, and (d) 4. No hysteresis loop was observed for S4 at all studied temperature region. Magnetization units are emu/g of total sample (iron oxide particles+alumina). Units on the insets are also emu/g for magnetization value and kilogauss for external magnetic field.

~4.5 nm, which as expected shows a magnetization saturation lower than S1, the core diameter varies from 2.16 to 3.12 nm, when the oxide thickness changes from 1.17 to 0.69 nm corresponding to a wt % Fe in the range of 15.7–46.36 wt %. The magnetization value of ~82 emu/g Fe observed for S3 is lower than for samples S1 and S2. This is attributed to a smaller particle size,[21] which leads to a higher contribution from the surface oxide layer and smaller contribution from a pure Fe core. This fact is supported by the results in Ref. 21, where the magnetization decreases linearly when plotted against the inverse of the radius of small Fe particles, showing that the magnetization is influenced by the surface of the particles. Indeed, the lack of magnetization saturation for S3 up to an external field of 55 kG indicates a dominant presence of smaller particles and the noncollinear spin structure of these small particles.[23–25] Similarly, we conclude that sample S4 shows paramagnetic behavior in all studied temperature range (5–300 K) due to the very fine particles (smaller than those of sample 3) with likely dominant iron oxide phase (large surface contribution) and noncollinear magnetic structure.

Thus, the initial catalyst particles, with diameters related as $d_1 > d_2 > d_3 > d_4$ have a core-shell structure Fe–(Fe–O), with contribution from the oxide layer increasing with the decrease of particle size.

The catalyst particle composition can also be independently verified from the blocking temperature (T_B), as it is related to the magnetic anisotropy energy (K), which is sensitive to particle structure and composition, by the expression[26]

$$T_B = K\langle V\rangle/25k_B, \tag{1}$$

assuming that particles are spherical and uniaxial. K is the magnetic anisotropy constant, $k_B = 1.38 \times 10^{-23}$ J is the Boltzmann constant, and $\langle V\rangle$ is the volume of the particle. For S1, as the particle mean diameter was measured by TEM, the determination of T_B would allow us to estimate K. For estimation of T_B, the temperature dependence of the magnetization under zero field cooling (ZFC) and field cooling (FC) conditions was investigated, further confirming the superparamagnetism of these Fe nanoparticles (Fig. 3). The ZFC magnetization measurements showed a peak at $T_{max} = 74$ K, indicative of a characteristic blocking temperature for superparamagnetic particles. Above T_B, the noninteracting Fe nanoparticle showed zero remanence and zero coercivity because of the thermal energy that allows the magnetization to flip between easy directions surpassing the energy barriers at zero fields [Fig. 2(a)]. Below T_B, the thermal activation is no longer able to overcome the magnetic crystalline anisotropy of the Fe nanoparticles and becomes magnetically frozen. As a result, a magnetic loop appears on the plot of the magnetization versus the applied external magnetic field [Fig. 2(a) inset]. Using the average spherical particle size of ~8 nm

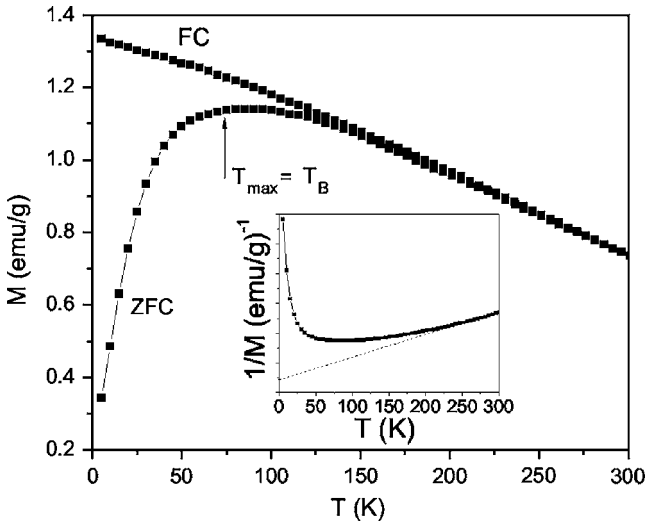

FIG. 3. Temperature dependence of the magnetization (M) curves under ZFC and FC (200 Oe) for S1. The inset is the thermal variation of $1/M$ under ZFC showing interacting particles in S1.

estimated from TEM images, the T_B value of 74 K, and Eq. (1), we obtained the effective uniaxial anisotropy constant value of $K=1.96\times10^6$ ergs/cm^3. This value of K is larger, by an order of magnitude, than for pure Fe ($\sim4.5\times10^5$ ergs/cm^3) and pure Fe oxide (4.4×10^4 and 1.2×10^4 ergs/cm^3 for 8.3 and 6.5 nm particles, respectively[28,29]). On the other hand, the obtained value is close to previously published results for small particles with pure Fe core coated with oxide layer[21] (K varies from 2.1×10^6 until 4.9×10^6 ergs/cm^3 when particle core size changes from 3.3 to 12.1 nm, respectively) obtained from the law of approach to saturation.[27] This again confirmed the core-shell structure of our initial catalyst particles. It is important to notice that, experimentally obtained values of effective anisotropy constant result from combined contributions (magnetocrystalline anisotropy, shape anisotropy and surface anisotropy). Therefore, the reason for the slight discrepancy could be partly explained by the core-shell structure of the particles, which, along with shape anisotropy and surface anisotropy, may add shell contribution because of surface strain.[21,23]

B. Magnetic characterization of catalyst after SWNT growth

The magnetization curves for all samples after carbon SWNT growth are shown in Fig. 4. As one can see, the growth of carbon SWNTs resulted in a superparamagnetic-ferromagnetic phase transitions for S1, 2, and 3, while the S4 showed a paramagnetic-superparamagnetic transition. The ferromagnetic nature of the nanoparticles in samples S1, 2,

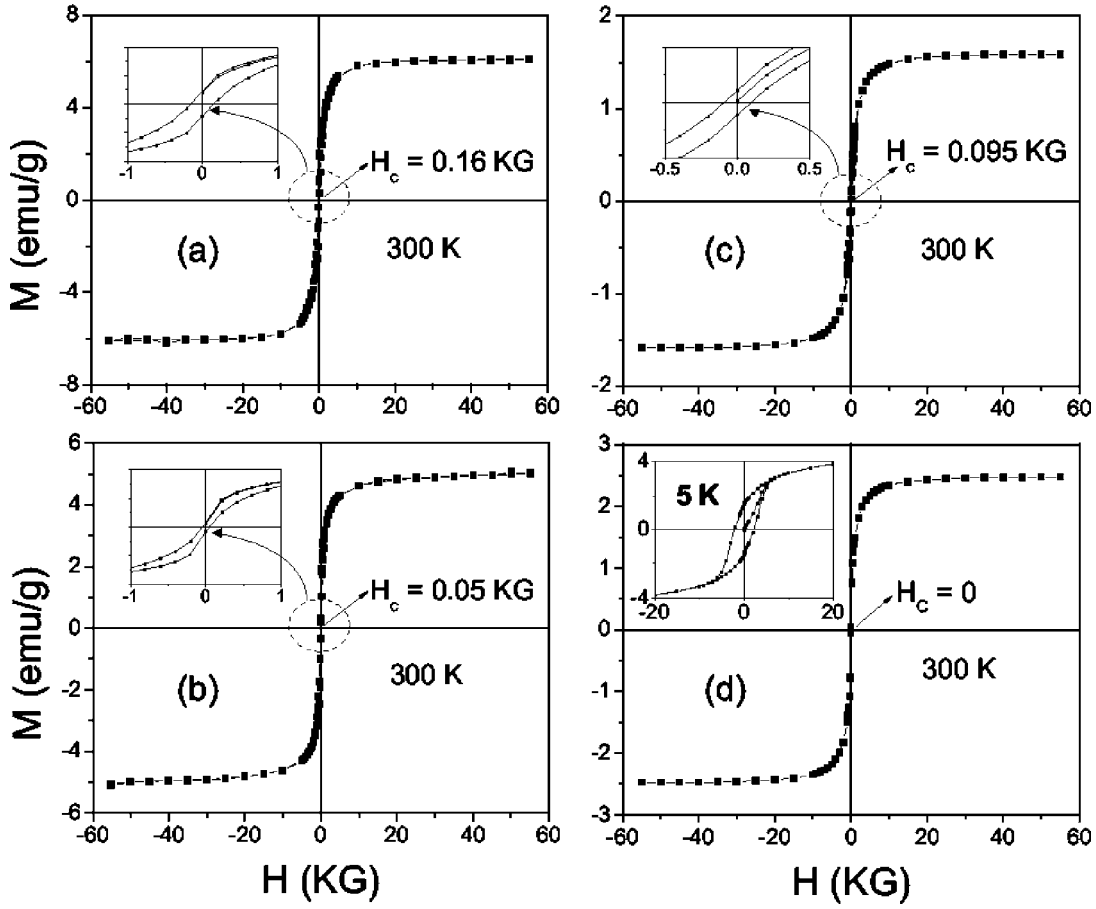

FIG. 4. Magnetization curves of the alumina supported Fe particles after carbon SWNT growth corresponding to samples (a) 1, (b) 2, (c) 3, and (d) 4. Only catalyst S4 shows superparamagnetic behavior at temperatures lower than 300 K after nanotube growth. Units on the inset to panel (d) are emu/g for magnetization value and kilogauss for external magnetic field.

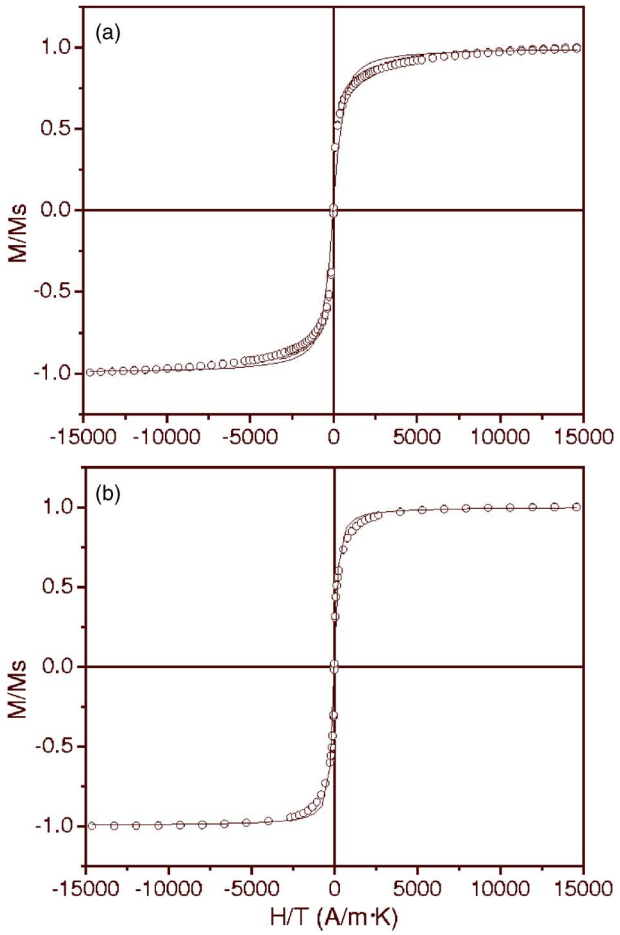

FIG. 5. The best fit for Langevin function for (a) catalyst S1 before carbon SWNT growth and (b) catalyst S4 after carbon SWNT growth.

and 3 is also indicated by the ratio of remnant to saturation magnetization at 5 K, which was $M_r/M_S \geqslant 0.5$. For S4 the $M_r/M_S \approx 0.18$ pointed to the superparamagnetic nature of nanoparticles. We attribute these phase transitions to an increase of particle size during SWNT growth for all four groups of catalyst.

As S1, 2, and 3 showed ferromagnetic behaviors up to 300 K, we were not able to estimate the average particle size for these catalysts after SWNT growth. However, it is possible to do it for S4, as it exhibited superparamagnetic behavior, from the plot of magnetization as a function of H/T using a Langevin function fitting,

$$M/M_S = \coth(\mu H/k_B T) - k_B T/\mu H, \tag{2}$$

where M_S is the saturation magnetization, μ is the true magnetic moment of each particle, k_B is the Boltzmann constant, and T is the absolute temperature. The magnetic moment μ is given by the relation of $M_S\langle V\rangle$, where $\langle V\rangle$ is the average particle volume. Thus, fitting of this data would give us the mean magnetic moment of our particles and, therefore, a mean particle diameter. For example, the magnetization data for S1 before nanotube growth revealed a moment $\mu \approx 5500\mu_B$ [Fig. 5(a)], which corresponds, assuming core-shell structure for the particles, to a mean diameter ~7.1 (±0.6) nm. This value is close to the result obtained by TEM (~8 nm). The discrepancy is attributed to magnetic interaction between particles, as it is clear from the thermal variation of $1/M$ under ZFC that obeyed the Curie-Weiss law (inset in Fig. 3) for temperature greater than 200 K. The best fit for the Langevin function for the sample 4 after SWNT growth is shown in Fig. 5(b). From this fitting, the mean magnetic moment per particle was found to be $\mu \approx 12\,500\mu_B$. For estimation of the mean particle size from the value of μ it is required to know its dominant phase composition. Because before nanotube growth the particles were rigorously reduced *in situ* at 500 °C using H_2/He mixed gas atmosphere we may exclude the presence of oxide layers. However, M_s for this sample is 130 emu/g, which is less than the value for pure iron indicating the presence of other possible phases. Formation of iron carbide phases during carbon SWNT growth has been discussed previously in the literature based on *in situ* TEM, Mössbauer spectra analysis, and magnetic properties.[30–34] Those studies concluded that the Fe–C alloy particles are possibly responsible for the nucleation and growth of the nanotubes. A detailed analysis of carbon nanotube formation mechanism using the Fe–C phase diagram was described in Ref. 35. These results are in good agreement with our recent studies,[36] where, using calorimetry measurements, we concluded the formation of iron carbide phases during carbon SWNT growth. The saturation magnetization of small iron carbide particles, including Fe_3C, Fe_5C, and Fe_7C_3 with 5–10 wt. % free carbon, reached 117 (Ref. 37 and 38) and 140 emu/g for bulk iron carbide.[39] By considering Fe_3C as a dominant phase on the particle (magnetization saturation ~120 emu/g at 300 K and density of 7.4 g/cm^3) we inferred a mean particle diameter from the Langevin fitting, Eq. (2), of $d \sim 5.8$ nm. Hence, even for S4, which has the lowest metal:support ratio (1:15), the catalyst particle mean size increased dramatically after nanotube growth becoming ~5.8 nm. Once particle size was known, we estimated the anisotropy constant from Eq. (1) and obtained a value of $K \sim 4.7 \times 10^6$ ergs/cm^3, considering $T_B \approx 150$ K ($T_{\max}$ for ZFC magnetization measurements in Fig. 6). The estimated value of K is of the same order as reported before for Fe–C nanoparticles ($K \sim 1.7 \times 10^7$ ergs/cm^3).[40] One distinction in the ZFC curve in Fig. 6 is a flat maximum located around 150±30 K, indicating a broad particle size distribution after carbon SWNT growth. This suggests that after carbon SWNT growth the catalyst particle size significantly increased with subsequent redistribution, resulting in a broadness of the size distribution. This is also accompanied with changes on the particle composition.

To understand the mechanism of the increase of catalyst particle size during SWNT growth, the magnetic characteristics of S4 were studied after heat treatment under analogous conditions than the synthesis, only without providing hydrocarbon (CH_4) gas (heat treatment under Ar gas flow at 820 °C). Comparison of Figs. 7 and 2(d) shows that there is no significant variation of the magnetic characteristics before and after the heat treatment of S4 under Ar gas flowing. There are some changes on the magnetization value at 5 *K* [inset of Fig. 2(d)], which could be attributed to the partial phase transitions of Fe oxide particles due to the heat treatment. Nevertheless, adding the methane gas resulted in nano-

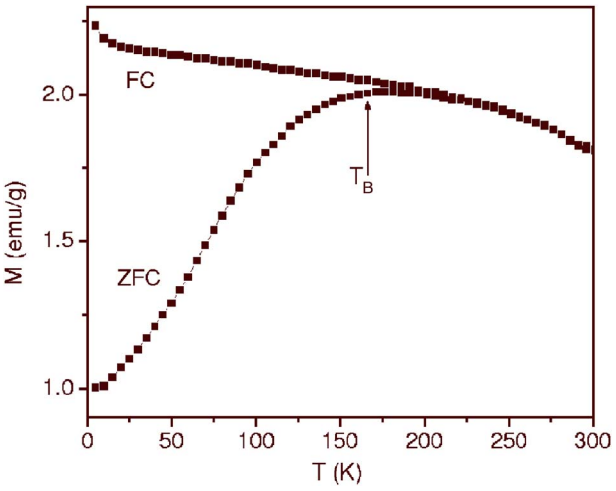

FIG. 6. Temperature dependence of the magnetization curves under ZFC and FC (200 Oe) for S4 after carbon SWNT growth.

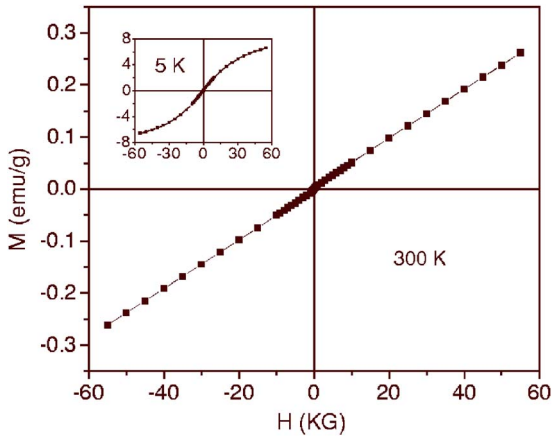

FIG. 7. Magnetization vs applied magnetic field for catalyst S4 at 5 and 300 K after heat treatment at 820 °C under H_2/Ar mixed gases flow.

tube growth and a paramagnetic-superparamagnetic phase transition [Fig. 4(d)]. In Ref. 36 and 41 based on calorimetry measurements combined with Raman spectroscopy measurements we showed that the growth of carbon SWNTs requires the liquefaction of the catalyst particles by carbon diffusion as an initial stage. Therefore, we attribute the increase of particle size during SWNT growth to the high mobility of the liquefied particles that resulted in their agglomeration. Our studies revealed that even in the case of molar ratios $Fe:Al_2O_3$ of 1:25 or 1:50, the growth of nanotubes still led to paramagnetic-superparamagnetic transition for the catalyst particles. Thus, even though the initial catalyst particle size can be very small, the growth of SWNTs resulted in a dramatic increase of their size. Consequently, the distance be-

TABLE I. Carbon SWNT diameters estimated from radial breathing mode (RBM) frequencies of Raman spectra. The diameters were estimated from $d=223.5/\omega_{RBM}-12$, where d is the tube diameter (nm) and ω_{RBM} the RBM frequency (cm^{-1}). The data with "+" are tubes which are out of resonance for particular laser excitation energy. The letters "vw," "w," "m," and "s" mean that the RBM signal is very weak, weak, moderate, or strong, respectively.

Catalyst	Laser excitation (nm)	Raman RBM frequency (cm^{-1})	Tube diameter (nm)
S1	1064	168w; 172m; 180m; 260w; 265w; 331m	1.43; 1.40; 1.33; +; +; 0.70
	785	150s; 175w; 195w; 236m; 263m	1.62; 1.37; +; +; 0.89
	647	212m; 220w	1.19; 1.07
	532	~250vw	0.94
	514.5	180w; 238vw; 262m	1.33; 1.00; 0.90
	488	186vw; 202w; 210w; 262m;	1.28; 1.17; 1.13; 0.89
S2	1064	168s; 176s; 262s; 311m; 329m	1.43; 1.37; +; 0.75; 0.71
	785	157vw; 164w; 263vs	1.55; 1.47; 0.89
	647	211m; 220w	1.19; 1.07
	532	165w; 177s; 187m; 195m; 210w; 226w; 247vs; 258w	1.46; 1.35; 1.28; 1.22; 1.13; 1.04; 0.95; 0.91
	514.5	~234vw; 260w	1.00; 0.90
	488	169vw; 179vw; 186w; 202w; 210w; 308w	1.42; 1.34; 1.28; 1.17; 1.13; 0.75
S4	1064	159vw; 180vw; 230w; 262s; 274vs; 285s; 308w	1.52; 1.33; +; +; +; 0.82; 0.75
	785	150s; 161vw; 175w; 195w; 206w; 236m; 263m	1.62; 1.50; 1.37; +; +; 1.00; 0.89
	647	174m; 192s; 212s; 222m; 250m; 260m; 280m; 295m	1.38; 1.24; 1.12; 1.06; 0.90; 0.83; 0.79
	532	165w; 177s; 187m; 195w; 210w; 226w; 247vs;	1.46; 1.35; 1.28; 1.22; 1.13; 1.04; 0.95;
	514.5	165m; 180m; 230w; 262m	1.46; 1.33; 1.03; 0.89
	488	162m; 180s; 203s; 258w	1.49; 1.33; 1.17; 0.91

tween initial catalyst particles and their interfacial tension value, for the given support material, are very crucial for controllable synthesis of small diameter carbon SWNTs by controlling the catalyst particle size. Redistribution of Ni catalyst particle size supported on amorphous carbon film during carbon SWNT growth was also reported in Ref. 42.

C. Raman studies

Finally, we discuss the relationship between catalyst particle size and the diameter of grown carbon SWNTs. In Table I, we display the SWNT diameters (d) synthesized using as catalyst S1, 2, and 4. The d were calculated from the expression $\omega_{\mathrm{RBM}}(d)=\alpha/d+\beta$, using the observed radial breathing mode (RBM) frequencies (ω_{RBM}) and the corresponding energies (E_{ii}) of interband transitions $v_i \rightarrow c_i$ determined on base of the plot of Kataura *et al.*,[43] with parameters γ_o =2.9 eV for the nearest neighbor carbon-carbon interaction energy and $a_{\mathrm{C-C}}=0.144$ nm for the nearest neighbor carbon-carbon distance. These parameters and the values α =223.5 cm^{-1} and $\beta=12.5$ cm^{-1} have been successfully applied for describing resonant Raman spectra of SWNTs.[44–46] The ω_{RBM} for different samples were obtained by Lorentzian or an appropriate sum of Lorentzian fittings of the breathing modes of Raman lines. We consider that only nanotubes with resonant energy window ($E_{\mathrm{laser}}\pm0.1$ eV) have a high probability for giving a strong signal in the Raman measurements.[47] As one can see from Table I, for all catalyst particles, the obtained SWNT diameters are in the range $0.70<d<1.71$ nm. TEM images taken on SWNTs exhibit also significant numbers of individual tubes with the diameters up to 8 nm, especially in the samples obtained on base of the catalyst with smaller particles (S4). We could not register the RBM from the tubes with big diameter due to the range limitation of the Raman spectrometers used. Considering a relationship between catalyst particle size and tube diameter of $R/d\sim1$,[2,13–15] the observation of nanotubes with big diameter when using the catalyst with the smallest initial particle size (S4) confirms that the particle size increased dramatically during the growth of the tubes. Nevertheless, we cannot exclude that small diameter tubes may also grow from large particles, e.g., nanotubes obtained using catalysts S1, 2, and 3, with particle mean diameter significantly bigger than S4, showed, after the tube growth, RBM peaks corresponding to very small diameter tubes (Table I). In Fig. 8, we show TEM images of the sample synthesized using catalyst S1, which had an initial particle size of ~8 nm. The images show SWNTs with a broad diameter distribution (1.3–7.5 nm) [Figs. 8(a) and 8(c)] and also multiwalled nanotubes [Fig. 8(b)]. The inset in Fig. 8(a) shows an example where the ratio between particle size and tube diameter is $R/d\sim1.6$. These observations point out that once the particle size is bigger than ~3 nm, the tube diameter may not necessary correlate with the particle size.

It is noticeable, that for the laser excitation of 647 nm very few RBM features are observed for nanotubes grown using relatively bigger initial catalysts, samples 1 and 2 ($\omega_{\mathrm{RBM}}=192$ and 212 cm^{-1}). The laser photon energy of 1.92 eV (647 nm) corresponds to transitions E_{22} and E_{33} of semiconducting tubes with diameters ~0.82 and ~1.64 nm and can also excite the E_{11} of metallic tubes. Thus, in the case of these catalysts the RBM intensity of the tubes responsible for mentioned transitions either is very weak (not

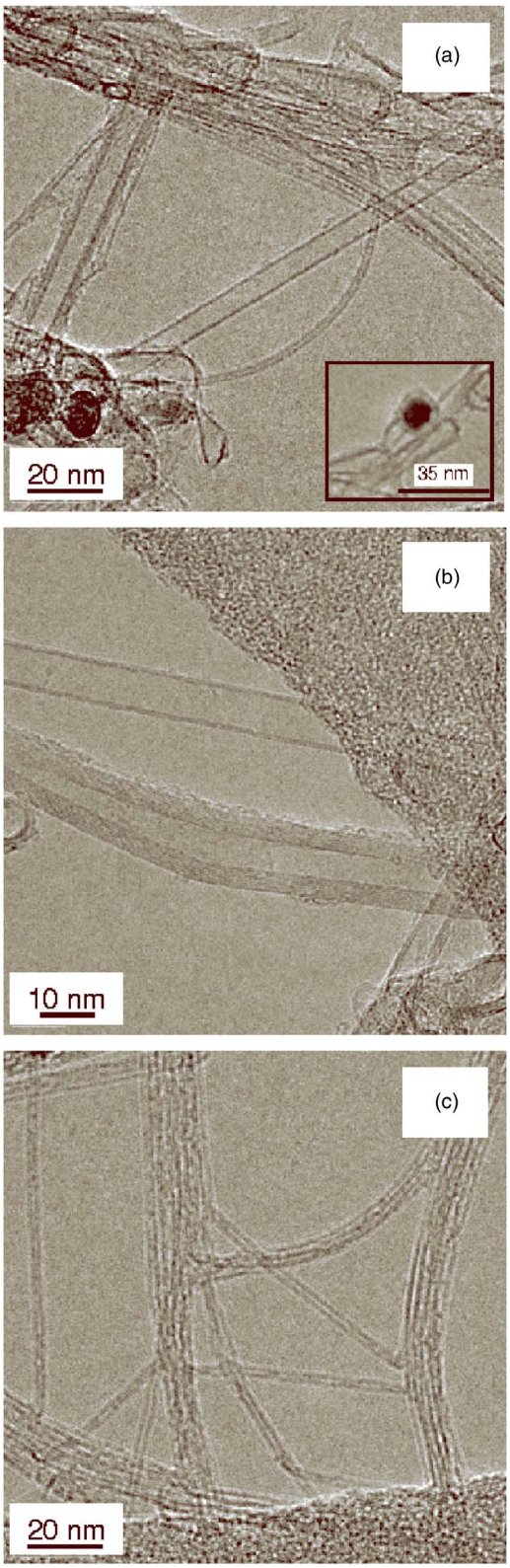

FIG. 8. TEM images of the carbon nanotubes synthesized using catalyst S1. The carbon material contains (a) very broad distribution of nanotube diameter, (b) SWNTs with big diameter and relatively thick walls, and multiwall nanotubes and (c) carbon SWNTs with different bundle sizes.

suitable for resonance) or very few tubes are present in the sample. In the meantime, well-resolved group of RBM peaks appeared in the spectra of sample 4 (smaller initial catalyst particles) corresponding to nanotubes with metallic E_{11} transition and E_{22} semiconducting transition.

IV. CONCLUSION

The SQUID magnetometer is a valuable tool for evaluation of catalyst particle size and composition before and after nanotube growth. The decrease of the catalyst/support ratio resulted in the formation of smaller particles (for the studied range) embedded in the support material. The magnetic data of the initial catalyst particles indicated a core-shell (Fe–Fe oxide) structure, with the volume fraction of shell contribution increasing when decreasing particle size. The growth of nanotubes leads to particle agglomeration with increase of their size, broadening of the size distribution, and formation of Fe–C phases. This becomes one of the main barriers to control the growth of small diameter SWNTs by controlling the initial catalyst size. Therefore, not only catalyst size and compositions are very crucial but also the interfacial interaction with the given support material. Finally, no direct correlation between catalyst size and nanotube diameters was found for big particles.

ACKNOWLEDGMENTS

One of the authors (A.R.H.) would like to thank Dr. G. Chen and Professor P. C. Eklund for supporting Raman measurements.

[1]K. Tanaka, T. Yamabe, and K. Fukui, *The Science and Technology of Carbon Nanotubes* (Elsevier, Oxford, 1999).
[2]H. Dai, A. G. Rinzler, P. Nikolaev, A. Thess, D. Colbert, and R. E. Smalley, Chem. Phys. Lett. **260**, 471 (1996).
[3]J. Kong, A. M. Cassell, and H. Dai, Nature (London) **395**, 878 (1998).
[4]J. H. Hafner, C. L. Cheung, and C. M. Lieber, Nature (London) **398**, 761 (1999).
[5]A. M. Cassel, J. A. Raymakers, J. Kong, and H. Dai, J. Phys. Chem. B **103**, 6484 (1999).
[6]A. R. Harutyunyan, B. K. Pradhan, U. J. Kim, G. Chen, and P. C. Eklund, Nano Lett. **2**, 525 (2002).
[7]B. Kitayanan, W. E. Alvarez, J. H. Harwell, and D. E. Resasco, Chem. Phys. Lett. **317**, 497 (2000).
[8]H. Hongo, M. Yudasaka, T. Ichihashi, F. Nihey, and S. Iijima, Chem. Phys. Lett. **361**, 349 (2002).
[9]A. Kasuya, Y. Sasaki, Y. Saito, K. Tohji, and Y. Nishina, Phys. Rev. Lett. **78**, 4434 (1997).
[10]A. Moisala, A. G. Nasibulin, and E. I. Kauppinen, J. Phys.: Condens. Matter **15**, S3011 (2003).
[11]A. A. Puretzky, H. Schittenhelm, X. Fan, M. J. Lance, L. F. Allard, Jr., and D. B. Geohegan, Phys. Rev. B **65**, 245425 (2002).
[12]A. R. Harutyunyan, G. Chen, and P. C. Eklund, Appl. Phys. Lett. **82**, 4794 (2003).
[13]S. B. Sinnott, R. Andrews, D. Qian, A. M. Rao, Z. Mao, E. C. Dickey, and F. Derbyshire, Chem. Phys. Lett. **315**, 25 (1999).
[14]Y. Li, W. Kim, Y. Zhang, M. Rolandi, D. Wang, and H. Dai, J. Phys. Chem. B **105**, 11424 (2001).
[15]C. L. Cheung, A. Kurtz, H. Park, and C. M. Lieber, J. Phys. Chem. B **106**, 2429 (2002).
[16]Y. Li and J. Liu, Chem. Mater. **13**, 1008 (2001).
[17]A. G. Nasibulin, A. Moisala, D. P. Brown, H. Jiang, and E. I. Kauppinen, Chem. Phys. Lett. **402**, 227 (2005).
[18]A. R. Harutyunyan, L. Grigorian, and T. Tokune, U.S. Patent No. 6,974,492 (3 March 2005).
[19]F. Chen, Y. Xue, V. G. Hadjiev, C. W. Chu, P. Nikolaev, and S. Arepalli, Appl. Phys. Lett. **83**, 4601 (2003).
[20]A. E. Berkowitz, W. J. Schuele, and P. J. Flanders, J. Appl. Phys. **39**, 1261 (1968).
[21]S. Gangopadhyay, G. C. Hadjipanayis, B. Dale, C. M. Sorensen, K. J. Klabunde, V. Papaefthymiou, and A. Kostikas, Phys. Rev. B **45**, 9778 (1992).
[22]M. Kishimoto, S. Kitahata, and M. Amemiya, IEEE Trans. Magn. **23**, 2818 (1987).
[23]L. Zhang, G. C. Papaefthymiou, and J. Y. Ying, J. Appl. Phys. **81**, 6892 (1997).
[24]J. M. Coey, Phys. Rev. Lett. **27**, 1140 (1971).
[25]P. M. A. de Bekker, E. De Grave, R. E. Vanderberghe, and L. H. Bowen, Hyperfine Interact. **54**, 493 (1990).
[26]J. S. Yin and Z. L. Wang, Phys. Rev. Lett. **79**, 2570 (1997).
[27]B. D. Cullity, *Introduction to Magnetic Materials* (Addison-Wesley, Reading, MA, 1972), p. 347.
[28]J. K. Vassiliou, V. Mehrotra, M. W. Russell, E. P. Giannelis, R. D. McMichael, R. D. Shull, and R. F. Ziolo, J. Appl. Phys. **73**, 5109 (1993).
[29]J. M. D. Coey and D. Khalafalla, Phys. Status Solidi A **11**, 229 (1972).
[30]H. Kim and W. Sigmund, Carbon **43**, 1743 (2005).
[31]P. Coquay, E. De Grave, R. E. Vandenberghe, C. Dauwe, E. Flahaut, C. Laurent, A. Peigney, and A. Rousset, Acta Mater. **48**, 3015 (2000).
[32]A. Peigney, P. Coquay, E. Flahaut, R. E. Vandenberghe, E. De Grave, and C. Laurent, J. Phys. Chem. B **105**, 9699 (2001).
[33]E. P. Sajitha, V. Prasad, S. V. Subramanyan, S. Eto, K. Takai, and T. Enoki, Carbon **42**, 2815 (2004).
[34]K. Teo, C. Singh, M. Chhowalla, and H. S. Nalwa, *Encyclopedia of Nanoscience and Nanotechnology*, edited by H. S. Nalwa (American Scientific Publishers, California, 2003), Vol. 1, p. 665.
[35]H. Kanzow and A. Ding, Phys. Rev. B **60**, 11180 (1999).
[36]A. R. Harutyunyan, E. Mora, and T. Tokune, Appl. Phys. Lett. **87**, 051919 (2005).
[37]S. Tajima and S. Hirano, Jpn. J. Appl. Phys., Part 1 **29**, 662 (1990).
[38]S. Hirano and S. Tajima, J. Mater. Sci. **25**, 4457 (1990).
[39]X. Q. Zhao, B. X. Liu, and Z. Q. Hu, J. Magn. Magn. Mater. **164**, 401 (1996).
[40]D. Babonneau, J. Briatico, F. Petroff, T. Cabioc'h, and A. Naudon, J. Appl. Phys. **87**, 3432 (2000).
[41]A. R. Harutyunyan, E. Mora, and T. Tokune, Appl. Phys. Lett. **86**, 153113 (2005).
[42]E. F. Kukovitsky, S. G. L'vov, N. A. Sainov, V. A. Shustov, and L. A. Chernozatonskii, Chem. Phys. Lett. **355**, 497 (2002).
[43]H. Kataura, Y. Kumazawa, Y. Maniwa, I. Umezu, S. Suzuki, Y. Ohtsuka, and Y. Achiba, Synth. Met. **103**, 2555 (1999).
[44]R. Saito, G. Dresselhaus, and M. S. Dresselhaus, Phys. Rev. B **61**, 2981 (2000).
[45]M. Milnera, J. Kurti, M. Hulman, and H. Kuzmany, Phys. Rev. Lett. **84**, 1324 (2000).
[46]S. M. Bachilo, M. S. Strano, C. Kittrell, R. H. Hauge, R. E. Smalley, and R. B. Weisman, Science **298**, 2361 (2002).
[47]A. Jorio, R. Saito, J. H. Hafner, C. M. Lieber, M. Hunter, T. McClure, G. Dresselhaus, and M. S. Dresselhaus, Phys. Rev. Lett. **86**, 1118 (2001).